Evidences on double Gaussian (DG) distribution of barrier heights in Au/(PVA-Fe_3O_4)/n-Si Schottky barrier diodes (SBDs) from the current-voltage (I-V) measurements in wide temperature

A. ARSLAN ALSAÇ[a,*], T. SERIN[a], Ş. ALTINDAL[b], Y. A. KALANDARAGH[c,d]
[a]*Ankara University, Faculty of Engineers, Department of Engineering Physics , 06900 Ankara, Turkey*
[b]*Gazi University, Faculty of Sciences, Department of Physics, 06900 Ankara, Turkey*
[c]*Department of Physics, University of Mohaghegh Ardabili, P.O. Box 179, Ardabil, Iran*
[d]*Department of Engineering Sciences, Sabalan University of Advanced Technologies (SUAT), Namin, Iran*

The I-V characteristics of Au/(PVA-Fe_3O_4)/n-Si SBDs were measured in wide-temperature (80-320K) to specify the possible conduction-mechanisms (CMs). Structural characterization of (PVA-Fe_3O_4) interlayer was done using (XRD) which, confirmed that the formation of Fe_3O_4 nanostructures has spinel cubic-crystal structure and space group. The mean-size of clusters was found as 50-200 nm and nanostructure-size was found less than 20 nm from the SEM images. The forward bias Ln(I)-V characteristics show that barrier-height (BH) increasing with increasing temperature whereas ideality-factor (n) decreases. Such changes in the BH and n with temperature was successfully explained by thermionic-emission theory with Double-Gaussian-distribution (DGD) of the BHs.

(Received January 12, 2021; accepted August 16, 2021)

Keywords: Current-voltage-temperature (I-V-T) characteristics, Double Gaussian distribution of barrier heights, Temperature dependence of surface states

1. Introduction

In recent years, organic based metal-semiconductor (MS) type SBDs have gained more attention in electronic and optoelectronic application since organic materials have low-cost, flexibility, low molecular weight per molecule and easy grown methods such as sol-gel, electrospinning, and atomic layer deposition (ALD) [1-10]. Usually insulator based SBDs suffer from an increase in the leakage current. In addition, they used an insulator layer grown by traditional methods such as thermal or wet oxidation and sputtering cannot a complete passivated the unwanted interface states/traps (N_{ss}/D_{it}), and dislocations [46-47]. But, the leakage current and N_{ss} can be decreased by using high-dielectric interfacial layers such as ferroelectric materials and metal or graphene doped organic materials [8-10]. In addition, among organic materials PVA has some excellent features such as long-relaxation time, charge storage capacity, high-dielectric strength (>1000 kV/mm) and low melting point to be fully-hydrolyzed with adhesive properties [3-7,10-15].

In order to better understand the possible current-conduction mechanisms (CCMs) such as thermionic emission (TE), tunneling (thermionic-field-emission (TFE) and field emission (FE)), generation-recombination (GR), tunneling via N_{ss}/D_{it}, Gaussian distribution (GD), and nature of barrier-height (BH) between metal and semiconductor both electric and dielectric measurement of these devices must be carried out in wide range of temperatures, bias voltage, and frequency. There may be simultaneous contribution from two or more CCMs especially at low temperature [44-45]. When these measurements are carried out only at one or narrow temperature/voltage/frequency, they cannot supply more information to us on the possible CCMs and the nature of BH [16-20]. The high-dielectric interlayer usage acts isolated metal to semiconductor, regulates the charge transitions, and also prevents interdiffusion. Then again, organics have a weak conductivity and low dielectric consult, but their conductivity can be improved by using a suitable rate metal doped.

Generally, the calculation of BH and ideality factor (n) based upon TE theory revealed an increment in BH and a decrement in n with increasing temperature. The alterations in two important parameters come of very apparent noticeably at low temperatures. Additionally, deviation from linearity occurs in the conventional Richardson plot at these low temperatures, and the calculation of the effective Richardson constant (A^*) maybe millions times lower than the theoretical value of it. Monitoring very high n values at lower temperatures cannot be interpreted only by the interlayer presence, N_{ss}, the level of doping donor or acceptor atoms. Therefore, recently, the decrease of n and increase of BH with decreasing temperature are interpreted by TE theory with single or double GD of the BHs at around mean BH at M/S [21-25]. The observed deviations from the ideal case or standard TE theory can be routed from various sources such as surface preparation,

fabrication precess, the nonhomogenities in the BH, interfacial layer, and doping concentration atoms, the existence of series resistance (R_s) and N_{ss} [26-29].

In this paper, we aimed to explain that the fabricated Au/(PVA-Fe_3O_4)/n-Si (MPS) type SBDs instead of conventional metal-insulator-semiconductor (MIS) type SBDs improved their performance. To this end the I-V data on both polarizations of them have been measured in wide temperature range of 80-320 K in order to get more information on the possible CCMs. The decrease in n and increase in BH with decreasing temperature was successfully described based upon TE theory with double GD of the BHs.

2. Experimental details

2.1. Materials and characterization

Ferrous chloride ($FeCl_2.4H_2O$) and ferric chloride ($FeCl_3.6H_2O$) were acquired from Merck. Sodium hydroxide (NaOH) and ammonia (NH_4OH) were obtained from Loba Chemie. Deionized–deoxygenated water was used throughout this study. The investigation of samples structural quality was made by X-ray diffraction (XRD) with a Cu-K_α (λ=1.5406 ˚A) radiation with a range of 2θ from 20 to 80°. A scanning electron microscope (SEM, LEO 1430vp) was utilized to analyze the morphology and particle size of these ferrite nanostructures. The nanostructures band-gap and the absorbance value were measured by the aid of UV-1800 Shimadzu UV-Vis spectrophotometer. Availing from Keithley2400 source-meter and JanisVPF-475 cryostat at ~10^{-3} Torr, the I–V measurements of the structure were completed. During the experiments, a microcomputer was used via IEEE-488 ac/dc converter.

2.2. Preparation of ferrite nanostructures

In a typical procedure, 10 ml of $FeCl_2.4H_2O$ (0.3 M) and 10 ml of $FeCl_3.6H_2O$ (0.6 M) were prepared and mixed with each other. Then 6 ml of ammonium hydroxide solution (NH_4OH) was added to 100 ml of deionized water that was located into the bottom of round flask that was deoxygenated by bubbling N_2 gas. During the string of ammonium hydroxide solution by ultrasound and passing argon gas from the solution, the mixture of cations was added to it drop-by-drop. After 30 minutes, a black precipitate instantly appeared, which is detached and washed with a few drops of ammonium hydroxide solution and distilled water and then dried at room temperature.

2.3. Fabrication process of Au/(PVA-Fe_3O_4)/n-Si (MPS) type SBDs

Au/(PVA-Fe_3O_4)/n-Si SBDs were fabricated on Phosphore-doped (n-Si) single Si wafer with (100) orientation, ~350 μm thickness, 2 inch diameter, and 1-10 Ω cm resistivity. Above all, cleaning process of the wafer was started by using 55 °C acetone, continued by 18 MΩ.cm resistivity of methanol and distilled water and finalized in a H_2O, H_2O_2, and NH_4OH (65:13:13) solution at 70 °C and a HF: H_2O (1:24) solution. Later, a distilled water was used to wash the wafer and the wafer was located into the deposition chamber. After this process, sputtering was utilized for deposition of 99.999% pure Au with ~1500Å thickness through the n-Si wafer's entire back surface at nearly 10^{-6} Torr pressure, to achieve good ohmic contact formation. The next natural step, the deposition of PVA-Fe_3O_4 composite on the n-Si wafer's front surface, was realized by utilizing the spin coating method.

After growth of this organic layer, circular dots with 1mm diameter and 150 nm thick high pure Au rectifying contacts were formed on the (PVA- Fe_3O_4) composite layer through a metal shadow mask by high-vacuum thermal evaporation at 10^{-6} Torr. In this way, the fabrication of Au/n-Si SBDs with (PVA: Fe_3O_4) organic interlayer were completed. The schematic profile of the structure is presented in Fig. 1.

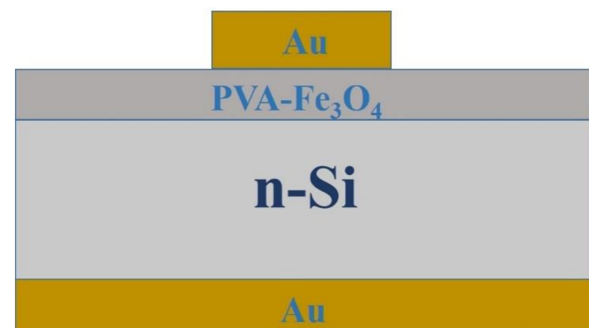

Fig. 1. The schematic diagram of diode (color online)

3. Results and discussions

3.1. X-ray diffraction

The XRD spectra of Fe_3O_4 nanostructures is shown in Fig.2. The diffraction spectra can be well indexed to spinel phase Fe_3O_4 reported in ICDD card (NO. 1111-01). In this spectra, the peaks belong to planes (111), (220), (311), (222), (400), (422), (511), (440), (620), (533), (444), (642), (731), (800), (751), (840), (931), (844) and (951), which confirmed the formation of Fe_3O_4 nano-structures with spinel cubic crystal structure. The space group is Fd-3m [31]. Also, the planes (221) and (222) are related to γ-Fe_2O_3 [32]. The crystallite size (D) of the prepared samples calculated about 13 nm from the Debye Scherrer equation (Eq.1).

$$D=k\lambda/\beta\cos\theta \quad (1)$$

where, the Scherer constant (~0.9), the full-width at half-maximum of the diffraction peak (FWHM), and the Bragg diffraction angle were denoted by k, β and θ respectively. λ is the X-ray wavelength of the Cu-Kα source and equal to 1.54056 Å.

3.2. SEM analysis

Fig.3. (a,b) shows the scanning electron microscope images of Fe_3O_4 nanostructures with distinct magnifications. According to Fig.3, nanostructures and nanoclusters can be distinct and nanoparticles have a nearly uniform distribution. Also, Fe_3O_4 nanostructures have a spherical shape, and due to their magnetic properties, the attraction generated between them leads to cluster formation [33]. The mean size of clusters was between 50-200 nm and the nanostructure size was less than 20 nm.

3.3. UV-Visible spectroscopy

The optical features of the samples were studied by UV-Vis absorption spectra, as presented in Fig.3 The optical energy band gap is obtained by relation [33]:

$$\alpha h\nu = c(h\nu - E_g)^m \qquad (2)$$

where, α, C, hν and E_g are the optical absorption coefficient, constant proportional, photon energy, and the band gap energy, respectively. [34]. Having both direct and indirect band gaps, the direct transition m = 2 and indirect transition in the relation were taken for iron ferrites. The band gap values for direct and indirect transitions are 2.2 eV and 1.4 eV respectively.

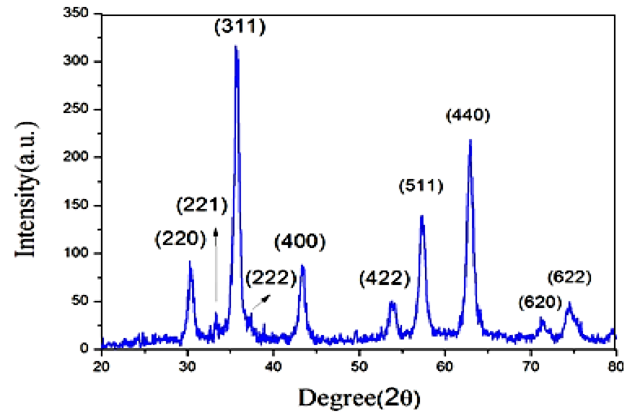

Fig. 2. XRD spectra of Fe_3O_4 nanostructures prepared by the ultrasound-assisted method (color online)

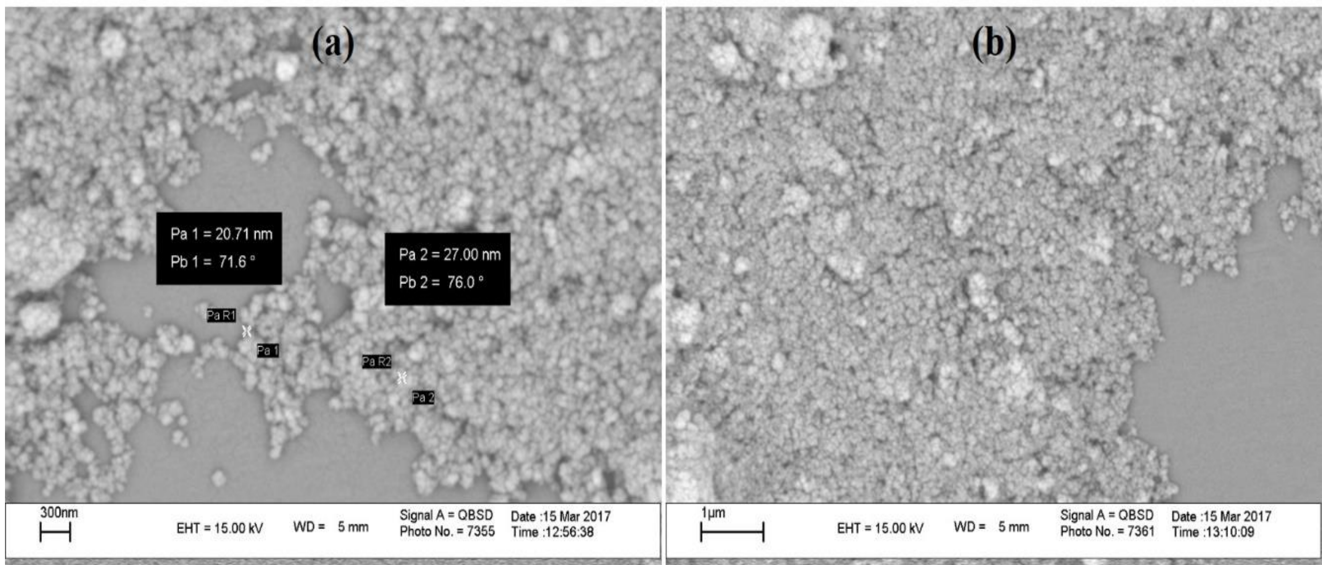

Fig. 3. SEM images of Fe_3O_4 nanostructures (a) 50kx (b)30kx

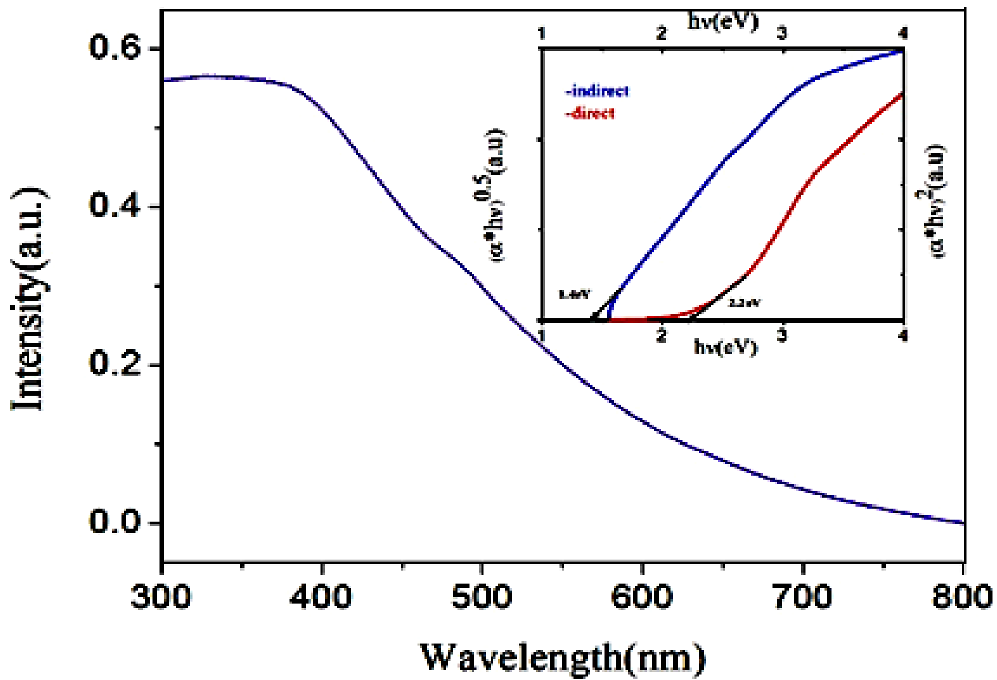

Fig. 4. Absorption spectra and Tauc plots for the sample (color online)

3.4. Current-voltage characteristics

Fig. 5 presents lnI-V curves of the MPS type SBDs between 80-320 K by 20 K steps. MS type structure's, with and without an interlayer, *I-V* characterization on forward biases can be well described by standard TE theory (V≥3kT/q) as follows:

$$I = AA^{*}T^{2}\exp\left(-\frac{q\Phi_{B0}}{kT}\right)\left[\exp\left(\frac{q(V-IR_{S})}{nkT}\right)\right] \quad (3)$$

Here A, A*, T, Φ_{B0}, n, and IRs are the diode area, effective Richardson constants (=112 A.cm^{-2} K^{-2} for Si), temperature in K, zero-bias barrier height (BH), and voltage drop on the R_s, [35,36]. Fig. 5 indicates, the forward biases lnI vs V curves display a good linear behavior in the intermediate bias region (0.075<V<0,35) and then deviated from the linearity at sufficiently high forward biases (V≥0.8V) due to the R_s effect in an organic interlayer [9,29,35,37].

The reverse saturation current (I_0) was extracted from lnI-V curve's linear part at V=0 for each temperature. Therefore the value of Φ_{B0} was estimated by using the diode area (A) and obtained from experimental value of I_0 by employing following relationship for each temperature:

$$\Phi_{B0} = \frac{kT}{q}\ln\left[\frac{AA^{*}T^{2}}{I_0}\right] \quad (4)$$

Then again, n was determined from the slope of lnI-V plot's linear part as follows:

$$n = \frac{q}{kT}\left(\frac{dV}{d(\ln(I))}\right) \quad (5)$$

The acquired values of I_0, n and Φ_{B0} of the Au/(PVA-Fe_3O_4)/n-Si SBD are tabulated in Table1. As can be seen Table1, these values were changed from 2.1x10^{-9} A, 9.846, 0.250 eV (at 80K) to 7.7x10^{-9} A, 2.060, 0.828 eV (at 320K), respectively. Such higher n values at lower temperatures can be ascribed by the electronic charges (electrons and holes) flowing through the lower barriers [20-24, 37]. But then, the n value, even at high temperatures, can be attributed to the presence of organic interlayer and a special density distribution of surface states (N_{ss}) [35-37]. As shown in Table 1 and Fig.6, while the value of n increases by temperature decrement, the value of Φ_{B0} decreases, and these changes both in the and Φ_{B0} become more significant particularly at low temperatures (T≤200K).

Table 1. The temperature dependent parameters values of the structure acquired from the forward biases I-V data

T (K)	I_0 (A)	n	Φ_{B0} (eV)	nT (K)	R_S (Ω)
80	2.1 x 10^{-9}	9.846	0.250	788	3.01 x 10^4
100	2.0 x 10^{-9}	7.505	0.250	751	2.64 x 10^4
120	1.9 x 10^{-9}	5.886	0.305	706	2.56 x 10^4
140	1.9 x 10^{-9}	4.922	0.359	689	2.53 x 10^4
160	2.0 x 10^{-9}	4.212	0.413	674	2.37 x 10^4
180	1.9 x 10^{-9}	3.508	0.469	631	2.35 x 10^4
200	2.0 x 10^{-9}	3.055	0.524	611	2.34 x 10^4
220	2.3 x 10^{-9}	2.756	0.578	606	2.25 x 10^4
240	2.9 x 10^{-9}	2.552	0.629	612	2.05 x 10^4
260	3.5 x 10^{-9}	2.372	0.681	617	2.04 x 10^4
280	4.6 x 10^{-9}	2.248	0.730	629	1.99 x 10^4
300	6.2 x 10^{-9}	2.174	0.778	652	1.99 x 10^4
320	7.7 x 10^{-9}	2.060	0.828	659	1.99 x 10^4

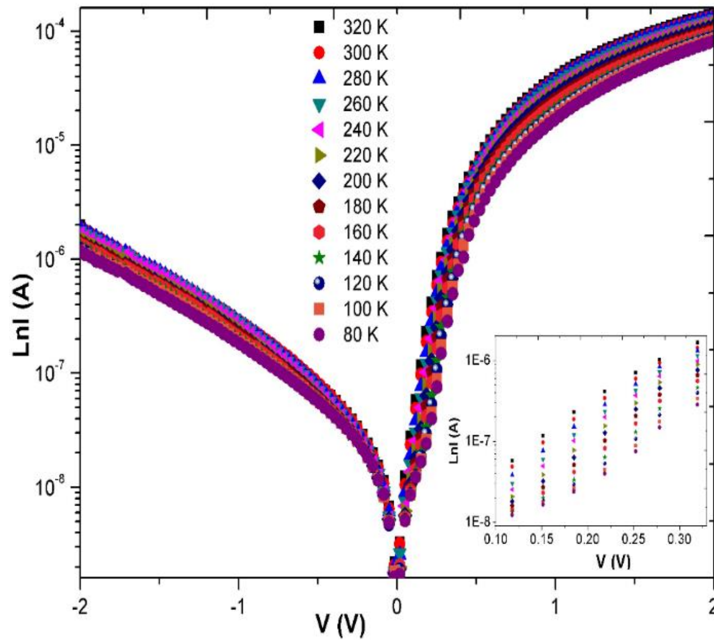

Fig. 5. The lnI-V curves of the Au/(PVA-Fe_3O_4)/n-Si SBD (color online)

Such behavior of them, show that the current conduction becomes dominant by the current flowing through the lower barrier/patches or pinch-off and so leads to the increase of ideality factor. This pinch-off was firstly proposed by Tung [39]. and this model was successfully used in the analysis of the CCMs in various Schottky type structures or diodes [1,2,6]. Then again, when temperature increases, gradually carriers gain adequate energy to easily overcome from the higher barriers. Additionally, such temperature dependence of Φ_{B0} is in obvious disagreement with the reported negative coefficient of the BH or the forbidden bandgap of a semiconductor Si. In addition, the increase in BH with increasing temperature is clearly not in treaty with the reported forbidden band gap's negative temperature-coefficient ($\alpha=\Delta Eg/\Delta T=-4,73x10^{-4}$ eV/K) of semiconductor (Si) and BH in the ideal case. Such behavior of Φ_{B0} with temperature and higher n values at lower temperature is a proof of the deviation from the standard TE theory, and so the other some CCMs such as tunneling (TFE and FE) and multistep tunneling via N_{ss} or dislocations may be dominated [36-38].

Tunneling mechanism can be dominant just at lower temperature and higher doping level of the semiconductor. Therefore, the high-doped semiconductors, depletion width comes of very thin and thus many charges can be passed through BH at low temperatue and so leads to an increasing in the n. But then, at higher temperatures, these carriers with enough energy which is higher than the Fermi-energy (E_F) level can be easily passed from semiconductor to the metal without tunneling over the barrier. In other words, FE and TFE theories can be occurred only in degenerate semiconductor ($N\geq10x10^{17}$

cm^{-3}). In theory, the measure of tunneling is determined by E_{oo} parameter and is given as follows [36,38].

$$E_{oo} = \frac{h}{4\pi}\left(\frac{N_D}{m_e{}^*\varepsilon_s}\right)^{1/2} \quad (6a)$$

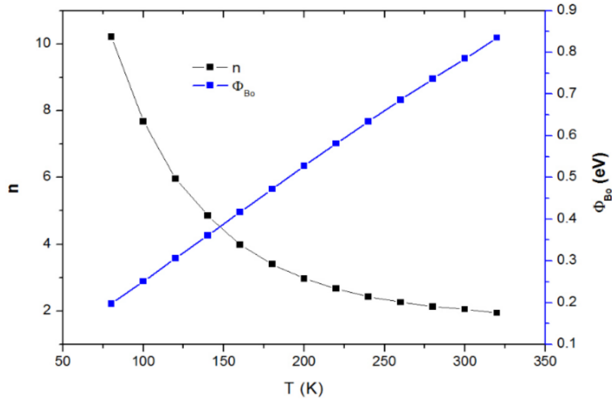

Fig. 6. The change of Φ_{B0} and n with temperature for the Au/(PVA-Fe_3O_4)/n-Si SBD calculated from forward bias I-V data (color online)

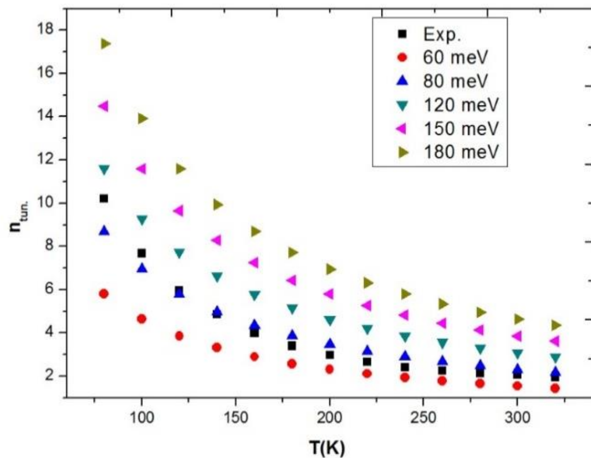

Fig. 7. The plot of $n_{tun.}$ vs T (K) (color online)

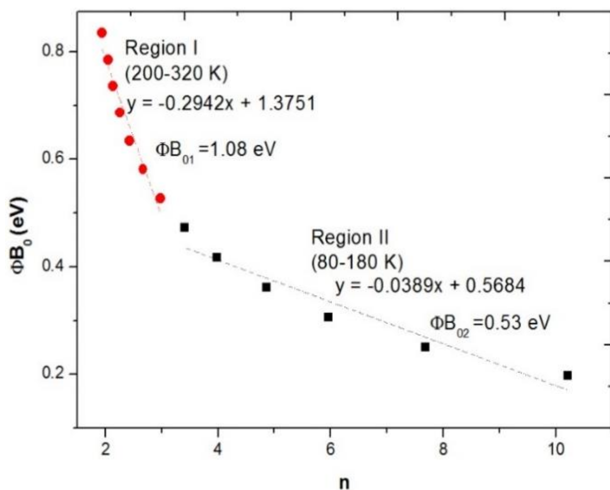

Fig. 8. Φ_{B0} vs n plots of the structure between 80-320 K (color online)

$$E_0 = E_{oo}\coth\left(\frac{E_{oo}}{kT}\right) \quad (6b)$$

$$n_{tun} = \frac{E_{oo}}{kT}\coth\left(\frac{E_{oo}}{kT}\right) \quad (6c)$$

In Eq.6a, m_e^* is the effective mass of electrons and ε_s ($11.8\ \varepsilon_o$) is the semiconductor's permittivity and where ε_o = 8,85 x10^{-12} F/m is the free space permittivity. Specifying whether tunneling mechanism is dominant or not, the tunneling parameter (E_{oo}) can be compared with thermal energy (kT/q). If the value of E_{oo} is substantially lower than kT/q at high temperatures, TE theory, E_{oo} is closer to kT/q at intermediate temperature, TFE theory, and E_{oo} is higher than kT/q at lower temperatures then FE theory may be possible CCMs. E_{oo} was acquired as 1.05 meV by using N_d and m_e^* values as 4.31x10^{15} cm^{-3} and 0.98 m_o and m_o is the electron rest mass (9.1x10^{-31} kg). Obviously, this theoretical E_{oo} value is much lower than kT/q even at 80 K. Moreover, as can be seen in Fig.7 (n_{tun} vs T), the value of E_{oo} was found 80 meV by fitting experimental value of n_{tun} vs T. This E_{oo} = 80 meV value comply with a doping concentration of 2.15x10^{18} cm^{-3}. So, if the FE dominates, then the E_o (=nkT/q) will lie on straight line or almost remain constant at each temperature. In this circumstances, E_o is independent from temperature and E_o is equal to E_{oo}. In other words, when Ln(I_o) vs V plots in the intermediate bias region then nT becomes almost constant. But, as shown in Table 1, the nT becomes almost constant in intermediate temperatures (~160-320 K). These results show that both FE and multistep tunneling by way of N_{ss} may be dominant CCMs as well as Gaussian distribution [19-20, 28, 29]:

As a result, the observed increment in BH and decrement in n by temperature rise may be ascribed by the spatial dispersion presence of BH at M/S interface or tunneling via surface states because such higher n and lower Φ_{B0} values at inferior temperatures can't clarified only by the interfacial polymer layer, N_{ss}, and higher values of doping concentration. These lower barriers/patches or pinch-off become more effective on the CCMs especially at low temperature because of at low or intermediate temperatures may be easy to surmount these pinch-off and leads to higher values of n [21]. Since temperature increases, then many charges gain enough energy to surmount the mean BH and leads to increase of appearing BH [48]. Therefore, Tung's theoretical approach and Schmitsdorf et al. found a linear correlation between the appearing BH (Φ_{Bo}=$\Phi_{ap.}$) and $n_{ap.}$ [20,21]. In order to show some proof to the existence of GD of BH, Φ_{Bo} vs n, F_{Bo} vs q/2kT, (n^{-1}-1) vs q/2kT plots were drawn and represented in Figs. 8, 9, 10, respectively. All plots have two distinctive straight lines with distinct slopes which are suitable to lower and enough high-temperature range which are explained in the literature by a modified version of the TE theory with double GD [26-30].

According to GD model, the BH is not homogenous and a mean BH ($\overline{\Phi}_{B0}$) is given as the distribution function

in Eq. 7a, depending on the standard deviation (σ_S) [22-23].

$$P(\Phi_{B0}) = \frac{1}{\sigma_S\sqrt{2\pi}} exp\left[-\frac{(\Phi_B-\overline{\Phi}_{B0})^2}{2\sigma_S{}^2}\right] \quad (7)$$

In this case, Φ_{B0} and n are represented as apearent BH (Φ_{ap}) and apparent ideality factor (n_{ap}) and are derived from below expressions (8 and 9), respectively [24-25]:

$$\Phi_{ap}(T) = \overline{\Phi}_{B0} - \frac{q\sigma_{So}{}^2}{2kT} \quad (8)$$

$$\frac{1}{n_{ap}(T)} - 1 = \rho_2 - \frac{q\rho_3}{2kT} \quad (9)$$

Linear correlation between Φ_{B0} and n is clearly seen in Fig.8 for low and high temperature regions. In these two linear parts of the Φ_{B0} n, the mean value of BH was found 1.08 eV for n=1 for high temperatures (80-180 K) and be 0.53 eV for low temperatures (200-320 K).

Then again, the mean BH ($\overline{\Phi}_{B0}$) and σ_s values were derived from the interception and slope of the Φ_{B0} vs q/2kT plot as 1.326 eV and 0.168 V for high temperatures, 0.655 eV and 0.082 V for low temperatures, respectively. Similarly, the voltage deformation constants of BH (ρ_2 and ρ_3) were found at the interception and slope of the (n^{-1} vs q/2kT) plot as -0.195 V and 0.0163 V for high temperatures, and -0.582 V and 0.00145 V for low temperatures, respectively.

Thus, the classical Richardson equation was modified by using the value of σ_s as follow.

$$\ln\left(\frac{I_0}{T^2}\right) - \frac{1}{2}\left(\frac{q\sigma_S}{kT}\right)^2 = \ln(AA^*) - \frac{q\overline{\Phi}_{Bo}}{kT} \quad (10)$$

Thereby, the modified Richardson plot was drawn by using Eq.10 and represented in Fig. 11. Modified Richardson plot has two distinct linear regimes with distinct slopes for low and high temperatures like Figs 8-10. A^* and $\overline{\Phi}_{B0}$ were derived from the interception and slope of the Fig. 11 as 77.21 A/(cmK)^2 and 1.0214 eV for inferior temperatures, 115.86 A/(cmK)^2 and 1.0635 eV for higher temperatures, respectively. It is quite obvious that, the obtained values of A^* from modified Richardson plot especially for high temperatures is very close to their theoretical value (112 A/(cmK)^2) for *n*-Si. Consequently, we can say that the CCM of Au/PVA-Fe_3O_4/n-Si SBD can be successfully clarified by DG distribution of BH rather than the others such as FE and multistep tunneling via surface states. Similar outcomes have already been achieved in the literature [24,26,29,40,41].

It is well known that many defects can be encountered during the fabrication of MS based devices which are called surface states or interface traps with energies located in the forbidden band gap (E_g) of semiconductor. This type of location can also be altered the performance of these devices. Therefore, the energy dependence of them were extracted by considering voltage-dependent n(V) and Φ_e(V). In application, the value of n deviated from the unity (ideal case) because of the interlayer presence, its thickness (d_i) and permittivity (ε_i), depletion layer width (W_D) or the density of doping concentration atoms as well as barrier inhomogeneities by following relations [11-a, 11-b].

$$n(V) = \frac{qV_i}{kT(I_i/I_0)} = 1 + d_i/\varepsilon_i\,(\varepsilon_s/W_D + qN_{ss}) \quad (11\text{-a})$$

$$\Phi_e(V) = [\Phi_{Bo} + (1 - 1/n(V))]V \quad (11\text{-b})$$

Additionally, for p-type semiconductor, the energy levels of N_{ss} relative to the higher edge of the valance band are given in Eq. 11-c:

$$E_c - E_{ss} = q(\Phi_e - V) \quad (11\text{-c})$$

$$N_{ss}(V) = \frac{1}{q}\left[\frac{\varepsilon_i}{d_i}(n(V) - 1) - \frac{\varepsilon_s}{W_D}\right] \quad (12)$$

Here; δ is the thickness of inter, $\varepsilon_i = 8\varepsilon_0$ is permittivity of the (PVA-Fe_3O_4) organic interlayer, ε_s = 11.8ε_0 is permittivity of of the Si.

Thus, the profile of N_{ss} vs (E_c-E_{ss}) plots was obtained for each temperature and represented in Fig. 12.

The calculated values of N_{ss} changed from ~10^{13} - 10^{14} $eV^{-1}cm^{-2}$ and decrease with increasing temperature and they increase from the middle of the E_g to the bottom level of E_v for all temperatures (Fig.12). The decrease of N_{ss} with temperature increment is the result of many charges escaped from the traps by gaining enough thermal energy. The shifting of their position towards to mid-gap (E_g) can be explained by the restructuring and reordering under temperature effect.

4. Conclusion

The I-V characterization of the Au/PVA-Fe_3O_4/n-Si structures at forward biases were examined between 80-320 K temperatures. Experimental outputs indicated that with increasing temperature the value of BH increased, whereas the value of *n* decreased. These behaviors may be caused by the variability of the obstacle height and the presence of interface states. The plots of Φ_{B0} vs n, Φ_{B0} vs q/2kT, (n^{-1}-1) vs q/2kT two different linear regions forp the HT (200-320 K) and LT (80-180 K). A * and Φ_{B0} acquired from the ln(I_0/T^2)-$q^2\,\sigma_0{}^2/2(kT)^2$ vs q/kT plot are 115 A/(cmK)^2 and 1.34 eV for HT region, 110 A/(cmK)^2 and 0.66 eV respectively. These results are consistent with the theoretical Richardson constant (112 A/(cmK)^2 for n-Si. Additionally, the acquired value of N_{ss}

is ~ 10^{13} $eV^{-1}cm^{-2}$ and this value can be noted compatible with a semiconductor device. The value of N_{ss} decreased with increasing temperature was explained many charges escaping from the traps by gaining enough thermal energy and the shifting of their position towards the mid-gap (E_g) was explained by the restructuring and reordering under temperature effect. In the light of I-V-T characterization results, the possible CCM in the Au/PVA-Fe_3O_4/n-Si SBD can be successfully attributed to DG distribution of BH rather than the others such as FE and multistep tunneling via surface states.

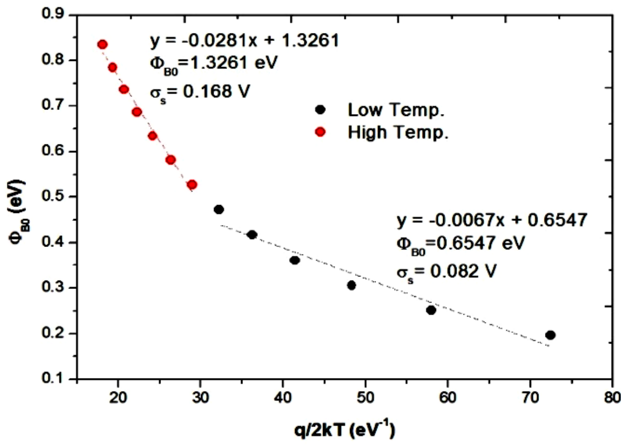

Fig. 9. Φ_{B0} vs q/2kT plot of the structure between 80-320 K (color online)

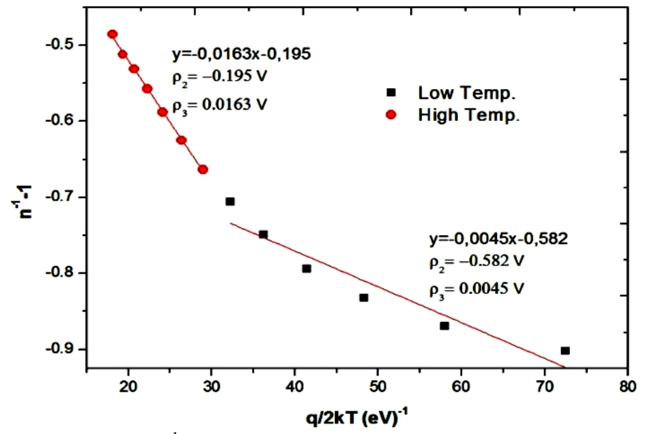

Fig. 10. n^{-1} -1 vs q/2kT plots of the structure between 80-320 K (color online)

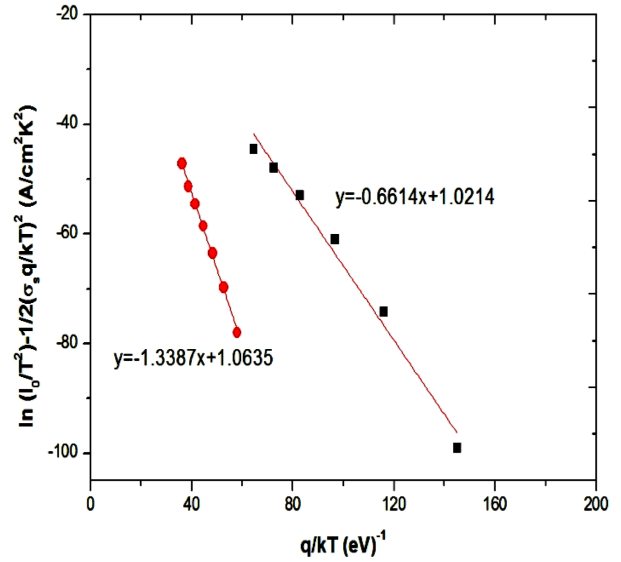

Fig. 11. The modified Richardson plots of the structure between 80-320 K (color online)

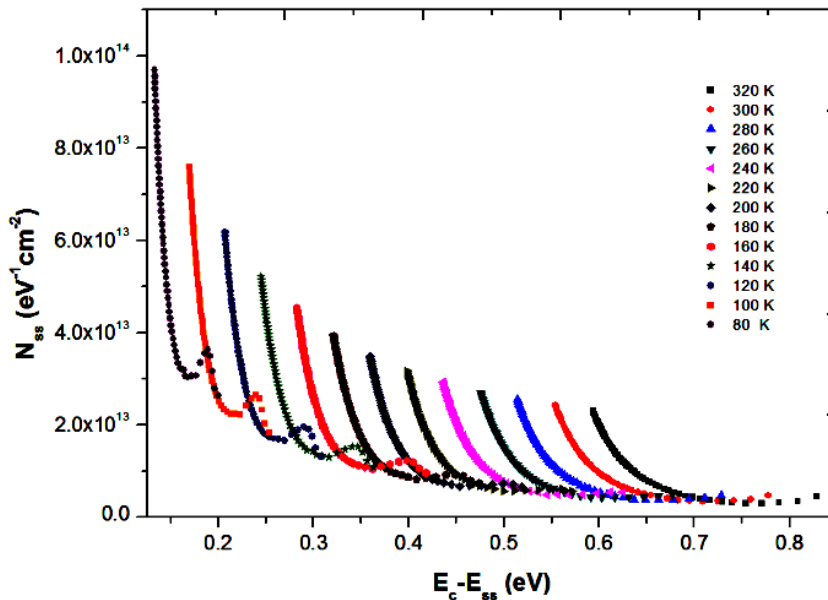

Fig. 12. The N_{ss} vs E_c-E_{ss} of the structure between 80-320 K (color online)

Acknowledgements

This study was supported by Gazi University Scientific Research Project. (Project Number: GU-BAP.05/2019-26).

References

[1] S. Boughdachi, Y. Badali, Y. Azizian-Kalandaragh, Ş. Altındal, J. Electron. Mat. **47**, 6945 (2018).
[2] M. Hussein Al-Daharob, H. Elif Lapa, A. Kökçe, A. Faruk Özdemir, D. Ali Aldemir, Ş. Altındal, Mat. Sci. Semicond. Proc. **85**, 98 (2018).
[3] L.A. Lipkin, J. W. Palmour, IEEE Trans. Elect. Devices. **46**, 525 (1999).
[4] T. Tunç, Ş. Altındal, İ. Dökme, H. Uslu, J. Elect. Mat. **40**, 157 (2011).
[5] S. Demirezen, Appl. Phys. A **112**, 827 (2013).
[6] S. Alialy, Ş. Altındal, E. E. Tanrıkulu, D. E. Yıldız, J. Appl. Phys. **116**, 083709 (2014).
[7] İ. Taşçıoğlu, U. Aydemir, Ş. Altındal, B. Kınacı, S. Özçelik, J. Appl. Phys. **109**, 054502 (2011).
[8] T. Tunç, I. Uslu, I. Dökme, S. Altındal, H. Uslu, Int. J. Polym. Mat. Polym. Biomater. **59**, 739 (2010).
[9] S. Altındal Yerişkin, M. Balbaşı, S. Demirezen, Indian J. Phys. **91**, 421 (2017).
[10] Ö. Vural, N. Yıldırım, Ş. Altındal, A. Türüt, Synt. Metal. **157** 679 (2007).
[11] H. C. Card, E. H. Rhoderick, J. Phys. D Appl. Phys. **4**, 1589 (1971).
[12] A. Kaya, İ. Yücedağ, H. Tecimer, Ş. Altındal, Mat. Sci. Semicond. Proc. **28**, 26 (2014).
[13] S. Alptekin, Ş. Altindal, J. Mat. Sci. Mat: Mat. Elect. **31**, 8 (2019).
[14] Y. Badali, A. Nikravan, Ş. Altindal, I. Uslu, J. Elect. Mat: Mat. Elect. **30**, 17032 (2019).
[15] S. Altındal Yerişkin, J. Elect. Mat. **47**, 3510 (2018).
[16] İ. Taşçıoğlu, S. Orkun Tan, F. Yakuphanoğlu, Ş. Altındal, J. Elect. Mat: Mat. Elect.**47**, 10(2018).
[17] H. Durmuş, M. Yıldırım, Ş. Altındal, J. Electron. Mat. Mat. Elect. **30**, 9029 (2019).
[18] B. Prasanna Lakshmi, M. Siva Pratap Reddy, A. Ashok Kumar, V. Rajagopal Reddy, Current Appl. Phys. **12**, 765 (2012).
[19] P. Singh, S. N. Singh, M. Lal, M. Husain, Sol. Energy Mat. Sol. Cells **92**, 1611 (2008).
[20] Y. P. Song, R. L. Van Meirhaeghe, W. H. Laflere, F. Cardon, Solid-States Elect. **29**, 633 (1986).
[21] T. Tung, Mat. Sci. Eng., R. **35**, 1 (2001).
[22] S. K. Chand, J. Appl. Phys. A **63**, 171 (1996).
[23] M. K. Hudait, K. P. Venkateswarlu, S. B. Krupanidhi, Solid-State Elect. **45**, 133 (2001).
[24] V. Rajagopal Reddy, V. Manjunath, V. Janardhanam, C. H. Leem, C. J. Cho, J. Elect. Mat. **44**, 549 (2015).
[25] J. P. Sullivan, R. T. Tung, M. R. Pinto, W. R. Graham, J. Appl. Phys. **70**, 7403 (1991).
[26] Ç. Ş. Güçlü, A. F. Özdemir, Ş. Altındal, Appl. Phys. A **122**, 1032 (2016).
[27] Y. Munikrishna Reddy, Indian J. Phys. **89**, 1161 (2015).
[28] Ö. Sevgili, S. Yılmaz, Ş. Altındal, E. Bacaksız, Ç. Bilkan, Proceedings of the National Academy of Sci. India Section A: Phys. Sci. **87**, 409 (2017).
[29] V. R. Reddy, V. Janardhanam, C. H. Leem, C. J. Choi, Superlattices Microstruct. **67**, 242 (2014).
[30] A. Eroglu, M. Yildirim, P. Durmus, I. Dokme. Appl. Polym. Sci. **137**, 48399 (2019).
[31] R. Sebastian, S., K. M. Maniammal, S. Xavier, E. M. Mohammed, J. Nano Research. **8**, 121 (2013).
[32] N. Tran, A. Mir, D. Mallik, A. Sinha, S. Nayar, T. J. Webster, Int. J. Nanomed. **5**, 277 (2010).
[33] R. D. Ambashta, M. Sillanpää, J. Hazardous Mat. **180**, 38 (2010).
[34] J. Tauc, R. Grigorovici, A. Vancu, Physica Status Solidi B **15**, 627 (1966).
[35] M. Sze, Physics of Semiconductor Devices, 2nd edn., Wiley, New York, 1981.
[36] B. L. Sharma, Metal-Semiconductor Schottky Barrier Junctions and Teheir Applications, Plenum Press-New York and London, 1984.
[37] İ. Taşçıoğlu, U. Aydemir, Ş. Altındal, B. Kınacı, S. Özçelik, J. Appl. Phys. **109**, 054502 (2011).
[38] F. A. Padovani, R. Stratton, Sol. State Elect. **9**, 695 (1996).
[39] R. T. Tung, Phys Rev B **45**, 13509 (1992).
[40] E. Özavcı, S. Demirezen, U. Aydemir, Ş. Altındal, Sens. Actuators A **194**, 259 (2013).
[41] S. Chand, J. Kumar, Semicond. Sci. Technol. **11**, 1203 (1996).
[42] Y. Zhong, G. Liu, M. Zhong, H. Wang, H. Li, J. Optoelectron. Adv. M. **14**(3-4), 245 (2012).
[43] E. Evcin Baydilli, A. Kaymaz, H. Uslu Tecimer, Ş. Altındal, J. of Elect. Mat. **49**, 7427 (2020)
[44] E. Evcin Baydilli, S. O. Tan, H. Uslu Tecimer, Ş. Altındal, Physica B: Cond. Mat. **598**, 412457 (2020).
[45] E. Evcin Baydilli, Ş. Altındal, H. Tecimer, A. Kaymaz, H. Uslu Tecimer, J. of Mat. Sci.: Mat. in Elect. **31**, 17147 (2020).
[46] H. Tecimer, Ş. Altındal, H. Aksu, Y. Atasoy, E. Bacaksız, J. of Mat. Sci.: Mat. in Elect. **28**, 7501 (2017).
[47] İ. Tascioglu, M. Ari., I. Uslu, S. Kocyigit, Y. Dagdemir, V. Corumlu, Ş. Altindal, Ceramics Int. **38**, 6455 (2012).
[48] C. S.Guclu, A. F. Ozdemir, Ş. Altındal, App. Phys. A **122**, 1 (2016).

*Corresponding author: aaysunalsac@gmail.com